Design of an Electrical Continuously Variable Transmission Based Wind Energy Conversion System

Yulong Liu, Shuangxia Niu, and Weinong Fu

***Abstract*—The electrical continuously variable transmission system is a very promising concept for variable-speed constant-frequency wind power generation due to its ability of seamless speed adjustment. In this paper, a novel wind energy conversion system based on electrical continuously variable transmission is proposed. This system combines the merits of two popular wind generation concepts: It enjoys high torque density like the permanent-magnet synchronous generator system and, also, it needs only a partial-scale converter like a doubly fed induction generator system. With a special doubly fed dual rotor structure, the system realizes both speed variation and power generation within one single machine, which makes it very compact. Besides introducing its structure and working principle, the design and performance analysis of the machine are presented in this paper. A prototype is made and tested for validation.**

***Index Terms*—Electrical continuously variable transmission (E-CVT), finite-element method (FEM), variable speed constant frequency (VSCF), wind energy conversion.**

I. Introduction

As an environmentally clean, renewable, and cost-effective energy source, wind power is of great significance for addressing the rising energy consumption and environmental problems. The increasing contribution of wind power generation has motivated rapid development of wind turbine systems in the past several decades.

The development of wind turbines has been well reviewed in literature [1]–[3]. Grid-connected wind turbines are often classified into the constant-speed constant-frequency (CSCF) concept and the variable-speed constant-frequency (VSCF) concept. Generally, the VSCF systems have higher power conversion efficiencies as they allow the turbine speed to vary and match the wind speed. For the VSCF concept, two solutions are popular, namely the doubly fed induction generator (DFIG) system and the direct-drive permanent-magnet (PM) synchronous generator (PMSG) system, as shown in Fig. 1(a) and (b). The main merit of the DFIG system is its low cost as no PM is used and it needs only a partial-scale converter, which is around 30% of the generator power level [4]. However, the additional mechanical gearboxes reduce the reliability of the DFIG system. In contrast, the direct-drive PMSG system has a high torque density and it does not need gearboxes or carbon brushes, which cause mechanical problems. However, the cost of the direct-drive PMSG system is much higher due to the use of PM material and the full-scale converter. It has also been investigated to realize the variable-speed operation using a mechanical torque/speed converter in [5] and [6]. This type of VSCF systems cost less as no power electronic converter is needed but they are rarely used in industry because of the issues related to the mechanical converter.

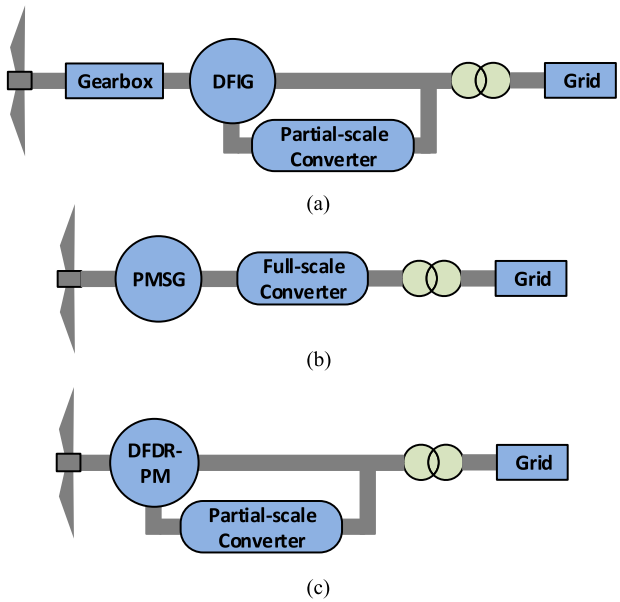

Fig. 1. Schematics of (a) DFIG system, (b) direct-drive PMSG system, and (c) proposed WECS.

Recently, the possibility of using electrical continuously variable transmission (E-CVT) systems for wind power generation has been investigated in [7]–[9]. In [7], an E-CVT system based on a planetary gear and a drive motor is proposed and it is connected to a generator for wind power generation. In [8], another design is proposed by replacing the planetary gear with a magnetic gear. However, these designs are quite bulky due to the multiple components. In [9], the speed variation is realized by a double-rotor machine, but this machine needs carbon brushes

This work was supported by the Research Grant Council, Hong Kong Special Ad-ministrative Region, China, under projects PolyU 152130/14E and PolyU 152202/15E.

The authors are with The Hong Kong Polytechnic University, Hong Kong (e-mail: iyulong2008@gmail.com; eesxniu@polyu.edu.hk; eewnfu@polyu.edu.hk).

as it has windings in a rotor and an additional synchronous generator is needed for power generation.

In this paper, a novel E-CVT based wind energy conversion system (WECS) is proposed. This WECS is gearless and it only needs a partial-scale converter as shown in Fig. 1(c). The most outstanding feature is that the variable-speed operation and power generation are realized within one single machine, which greatly reduces the size and simplifies the whole system. This machine has a doubly fed dual-rotor (DFDR) structure. By adjusting the frequency of the primary winding, a variable inner rotor speed is allowed, while the outer rotor speed is kept constant. In the meanwhile, it generates power by the electromagnetic interaction between the secondary winding and the outer rotor. As PM material is used for both the inner and outer rotor, the PM-excited machine has a relatively high torque density. By virtue of the flux-modulation effect, it can be designed-with a high pole-pair number (PPN) for direct-drive system. The gearless and brushless structure makes the machine reliable and maintenance free. After introducing the structure and working principle of the WECS, the finite-element method (FEM) based optimal design of this DFDR-PM machine is presented. The DFDR-PM is also prototyped and experiments are carried out to validate its performance.

II. Structure and Working Principle

A. Machine Structure and Working Principle

As the key component of the proposed WECS, the DFDR-PM machine is introduced first. A radial cross section of the DFDR-PM is shown in Fig. 2. It has two sets of windings, which are housed in one stator, and two coaxial rotors, which are in-stalled inside the stator. The inner rotor is a consequent-pole PM rotor in which all the PMs are magnetized in a radially outward direction. The outer rotor comprises interleaved PMs and steel segments. The secondary winding interacts with the outer rotor like a conventional single-rotor PM machine, and the primary winding interacts with both rotors through the flux-modulation effect. The flux-modulation effect means taking advantage of the harmonic components of the magnetic field [10]. In the proposed DFDR-PM machine, bidirectional flux modulation is employed.

Basically, in the airgap, the relationship between the magnetomotive force (MMF) drop F and the flux density B is

$$B = \lambda F \tag{1}$$

where λ is the permeance per unit area.

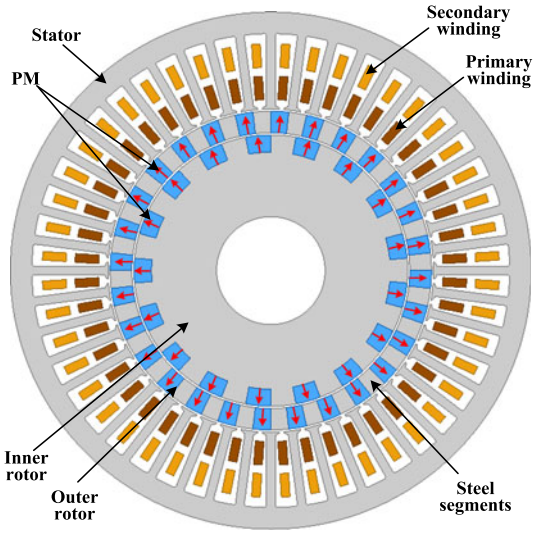

Fig. 2. Radial cross section of the DFDR-PM.

The MMF developed by the PM can be expressed as a sum of two components:

$$F \approx F_1 \cos[N_{\mathrm{ri}}(\theta - \omega_1 t) + \phi_1] + F_2 \cos[N_{\mathrm{ro}}(\theta - \omega_2 t) + \phi_2] \tag{2}$$

where F_1 and F_2 are the magnitudes of the MMF components due to the inner rotor and the outer rotor, respectively; N_{ri} and N_{ro} are the PPNs of the inner rotor and the outer rotor; ω_1 and ω_2 are the rotation speeds of the inner rotor and the outer rotor; and ϕ_1 and ϕ_2 are the initial phase angles of the two MMF components.

Similarly, the airgap permeance can be expressed as

$$\lambda \approx \lambda_0 + \lambda_1 \cos[N_{\mathrm{ri}}(\theta - \omega_1 t) + \phi_3] + \lambda_2 \cos[N_{\mathrm{ro}}(\theta - \omega_2 t) + \phi_4] \tag{3}$$

where λ_0 is the average value of λ; λ_1 is the magnitude of the alternating component due to the inner rotor; λ_2 is the magnitude of the alternating component due to the outer rotor; and ϕ_3 and ϕ_4 are the initial phase angles of the two alternating components, which are $\phi_3 = \phi_1 + \pi$ and $\phi_4 = \phi_2 + \pi$, as the PMs and steel segments are arranged alternately.

By substituting F and λ in (1) with (2) and (3), (4) can be deduced, as shown bottom of the page.

Obviously, the airgap flux density has six rotating components whose PPNs are N_{ri}, N_{ro}, $2N_{\mathrm{ri}}$, $2N_{\mathrm{ro}}$, $N_{\mathrm{ro}} - N_{\mathrm{ri}}$, and $N_{\mathrm{ro}} + N_{\mathrm{ri}}$, respectively. In a conventional PM machine, the $N_{\mathrm{ro}} - N_{\mathrm{ri}}$ component is negligible. But in the DFDR-PM, due to the

$$B \approx \left\{ \begin{array}{l} \lambda_0 F_1 \cos[N_{\mathrm{ri}}(\theta - \omega_1 t) + \phi_1] + \lambda_0 F_2 \cos[N_{\mathrm{ro}}(\theta - \omega_2 t) + \phi_2] \\ -\frac{1}{2}\left\{\lambda_1 F_1 \cos[2N_{\mathrm{ri}}(\theta - \omega_1 t) + 2\phi_1] + \lambda_2 F_2 \cos[2N_{\mathrm{ro}}(\theta - \omega_2 t) + 2\phi_2]\right\} \\ -\frac{1}{2}(\lambda_1 F_2 + \lambda_2 F_1) \left\{ \begin{array}{l} \cos\left[(N_{\mathrm{ro}} - N_{\mathrm{ri}})\left(\theta - \dfrac{N_{\mathrm{ro}}\omega_2 - N_{\mathrm{ri}}\omega_1}{N_{\mathrm{ro}} - N_{\mathrm{ri}}} t\right) + \phi_2 - \phi_1\right] \\ + \cos\left[(N_{\mathrm{ro}} + N_{\mathrm{ri}})\left(\theta - \dfrac{N_{\mathrm{ro}}\omega_2 + N_{\mathrm{ri}}\omega_1}{N_{\mathrm{ro}} + N_{\mathrm{ri}}} t\right) + \phi_2 + \phi_1\right] \end{array} \right\} \\ -\frac{1}{2}(\lambda_1 F_1 + \lambda_2 F_2) \end{array} \right\} \tag{4}$$

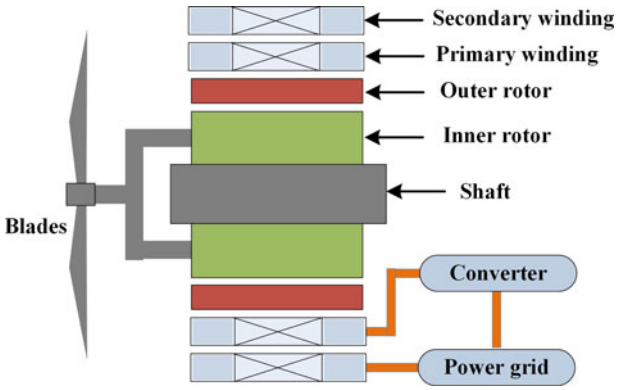

Fig. 3. Configuration of the proposed WECS.

existence of the steel segments, the $N_{\mathrm{ro}} - N_{\mathrm{ri}}$ component becomes significant. By designing the PPN of the primary winding to be

$$P_{\mathrm{pw}} = N_{\mathrm{ro}} - N_{\mathrm{ri}} \tag{5}$$

voltage will be induced in the primary winding with the rotors rotating. From (5), the rotation speed of the $N_{\mathrm{ro}} - N_{\mathrm{ri}}$ component is

$$\omega_{\mathrm{pw}} = \frac{N_{\mathrm{ro}}\omega_2 - N_{\mathrm{ri}}\omega_1}{N_{\mathrm{ro}} - N_{\mathrm{ri}}}. \tag{6}$$

Accordingly, the frequency of the induced voltage in the primary winding is

$$f_{\mathrm{pw}} = \frac{\omega_{\mathrm{pw}}(N_{\mathrm{ro}} - N_{\mathrm{ri}})}{2\pi} = \frac{N_{\mathrm{ro}}\omega_2 - N_{\mathrm{ri}}\omega_1}{2\pi}. \tag{7}$$

The configuration of the proposed WECS is depicted in Fig. 3. The inner rotor is fixed on the shaft, which is connected to the turbine blades. The primary winding is linked to the power grid through a converter and the secondary winding is linked to the power grid directly. Reforming (7), the speed of the outer rotor is

$$\omega_2 = \frac{N_{\mathrm{ri}}\omega_1 + 2\pi f_{\mathrm{pw}}}{N_{\mathrm{ro}}}. \tag{8}$$

When the blade speed ω_1 varies, by adjusting the excitation current of the primary winding, the speed of the outer rotor ω_2 can be kept constant. Hence, the frequency and amplitude of the induced voltage in the secondary winding are constant, enabling it to be directly connected to the power grid.

For the secondary winding, as it constitutes a conventional PM machine with the outer rotor, its PPN is the same to that of the outer rotor.

Fractional slot design is adopted to reduce the slot number for both windings. Concentrated winding is used by the secondary winding to reduce the copper loss. The pole–slot combination for fractional slot concentrated winding has been investigated in [11] and [12].

B. Energy Conversion

During stable operation, the mechanical torque from the turbine is balanced by the electromagnetic torque on the inner rotor T_{ri}. For the outer rotor, its torque T_{ro} comprises two electromagnetic components, namely the part due to the primary winding T_{ro1} and the part due to the secondary winding T_{ro2}. As the outer rotor is a floating rotor, the two torque components need to cancel each other, which means $T_{\mathrm{ro}} = T_{\mathrm{ro1}} + \mathrm{T}_{\mathrm{ro2}} = 0$. The torque relationship between the rotors in a flux-modulated machine has been introduced in [13], which in this machine is

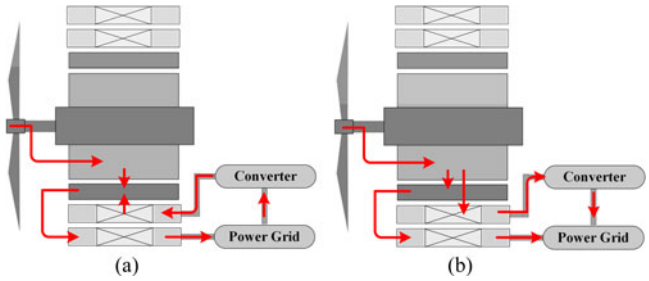

Fig. 4. Power flow in the WECS during (a) subsynchronous operation and (b) supersynchronous operation.

$$\frac{T_{\mathrm{ro1}}}{N_{\mathrm{ro}}} = \frac{T_{\mathrm{ri}}}{N_{\mathrm{ri}}}. \tag{9}$$

When the losses in the system are not considered, the input power of the converter is

$$P_{\mathrm{con}} = P_{\mathrm{rated}} - P_{\mathrm{wind}} = T_{\mathrm{ro1}}\omega_2 - T_{\mathrm{ri}}\omega_1 \tag{10}$$

where P_{rated} is the rated power output to the power grid and P_{wind} is the wind power captured by the turbine blades. Clearly, only a partial-scale converter is needed for this WECS and its power level depends on the designed speed range of the turbine blades. Like that of a DFIG, a synchronous speed is defined for the inner rotor of the DFDR-PM as

$$\omega_{1\mathrm{syn}} = \frac{N_{\mathrm{ro}}}{N_{\mathrm{ri}}}\omega_2 = \frac{2\pi f_{\mathrm{sw}} N_{\mathrm{ro}}}{P_{\mathrm{sw}} N_{\mathrm{ri}}} \tag{11}$$

where f_{sw} and P_{sw} are the frequency and the PPN of the secondary winding, respectively. Accordingly, the speed below/above the synchronous speed is defined as subsynchronous/supersynchronous. The system working principle is simply introduced as follows:

1) When the inner rotor is rotating at the synchronous speed, P_{con} is 0, which means no power is flowing through the converter and the primary winding. The primary winding needs to be fed with dc current.
2) During subsynchronous operation, P_{con} is positive. The primary winding helps to drive the outer rotor and it extracts power from the grid through the converter as shown in Fig. 4(a).
3) During supersynchronous operation, P_{con} is negative. More power is supplied by the inner rotor than the rated power needed by the outer rotor. The extra power goes to primary winding for generation. Both the primary wind-ing and the secondary winding inject power to the grid. The power flow is shown in Fig. 4(b).

III. Preliminary Design Consideration

In view of the fact that the DFDR-PM is essentially a combination of an E-CVT and a generator, the performances of

both of them have to be considered. For convenience, the two components are referred to as E-CVT part and generator part, respectively.

Considering that T_{ro1} and T_{ro2} need to cancel each other, the E-CVT part and the generator part should have similar torque capability. As these two parts have the same rotor diameter, they should also have similar electrical load. As a result, in this design, the slot room is evenly divided by the primary winding and the secondary for the sake of heat dissipation.

Since the torques of the rotors are inversely proportional to their PPNs, as shown in (9), only the torque of the outer rotor needs to be considered for the design of the E-CVT part.

The cogging torque in a flux-modulated machine is decided by the cogging torque factor, which is the greatest common devisor between the PPNs of the two rotors [10], [14]. In the proposed DFDR-PM machine, the cogging torque factor is 1 with the designed pole combination and its cogging torque is expected to be relatively small.

For the design of a conventional synchronous machine, the following famous sizing equation is usually used:

$$S = 11K_w \cdot \bar{B} \cdot A \cdot D^2 \cdot l \cdot n \tag{12}$$

where S is the output power in W, K_w is the winding factor, $\bar{B}$ is the mean flux density in the airgap in T, A is the electrical loading in A/m, D is the airgap diameter, l is the core length, and n is the rotational speed [15]. For the DFDR-PM machine, although two windings are used, they do not affect each other, except for the saturation problem since their PPNs are different. Therefore, (12) can still be used to decide the preliminary geometric parameters with only the generator part considered.

The ratio of PM width to steel width in the rotor has been investigated in [16]. To achieve the best flux-modulation effect, this ratio should be 0.5–0.6. In the proposed DFDR-PM, the rotor PM and steel segments have the same width.

To have a general idea of the effect of the geometrical parameters on the torque performance of the DFDR-PM, a parametric analysis is first done before optimization. The analyzed variables are as follows:

1) H_{ri}, radial length of the PM in the inner rotor;
2) H_{ro}, radial length of the outer rotor;
3) R_s, inner radius of the stator;
4) H_y, radial length of the stator yoke;
5) W_t, width of the stator teeth.

For each variable, the effect on T_{ro1} and T_{ro2} is analyzed separately using a static two-dimensional FEM. The excitation current is fixed at the maximum torque point during the analysis. The analysis results, as shown in Fig. 5, are as follows:

1) As is analyzed in Section II, the inner rotor only interacts with the primary winding and the change of H_{ri} does not have significant influence on T_{ro2}. For the E-CVT part, the change of H_{ri} affects its MMF and the flux-modulation effect. T_{ro1} is maximized at a certain H_{ri} value.
2) To increase T_{ro2}, H_{ro} is required to be large enough, which is similar to the situation in a conventional PM machine. However, for the E-CVT part, which is basically a flux-modulated machine, the increase of H_{ro} not only increases the MMF, but also decreases the radius of the inner airgap and affects the flux-modulation effect. Therefore, a compromise is needed for the design of H_{ro}.
3) The effects of R_s on T_{ro1} and T_{ro2} are similar. The increase of R_{s} increases the airgap radius, which is a positive element for improving the torque. However, it also compresses the slot area, which decreases the electrical load considering a constant current density.

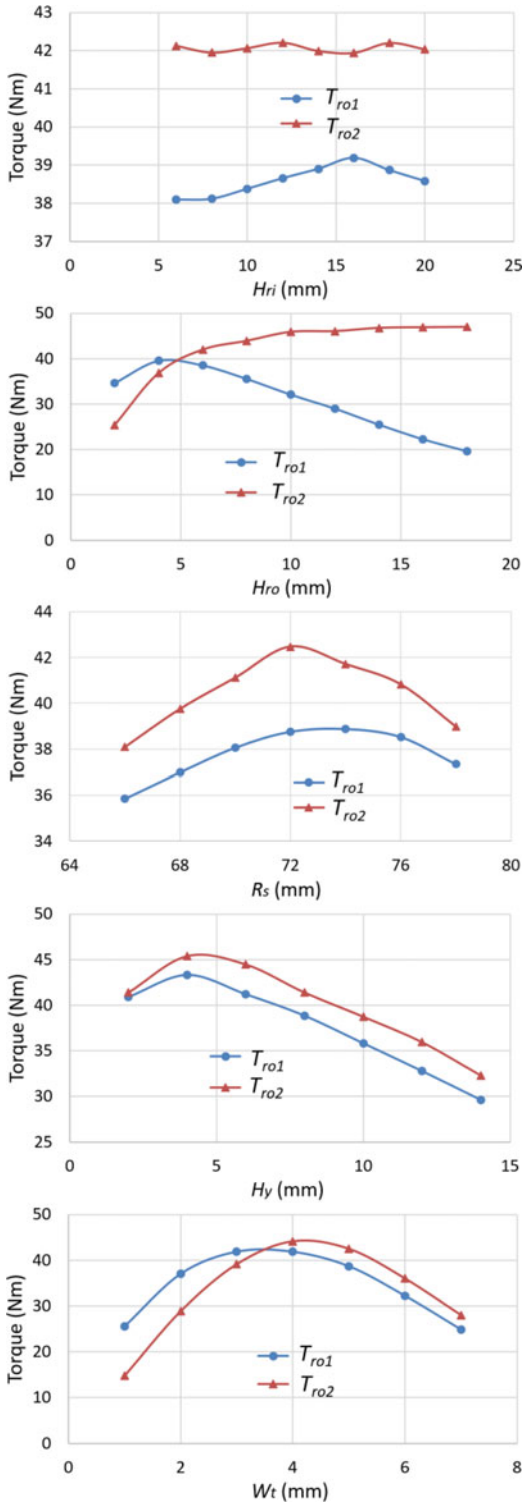

Fig. 5. Effect of geometric parameters on torque.

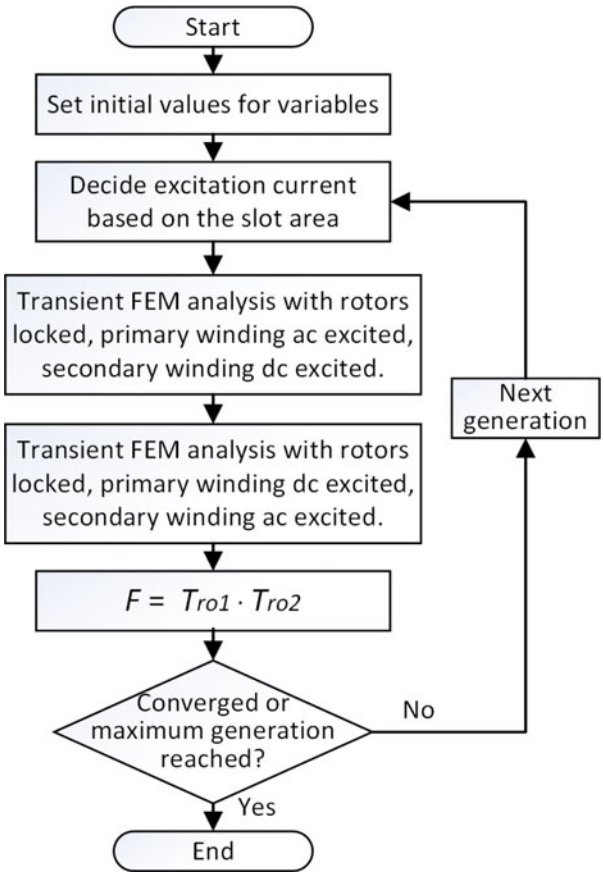

Fig. 6. Flowchart of the optimization process.

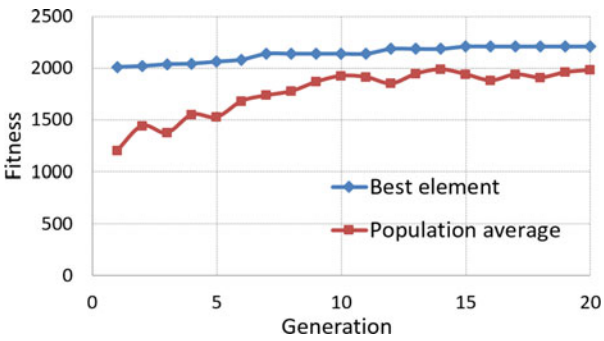

Fig. 7. Fitness variation during the optimization process.

4) The effects of H_y and W_t are similar. An increase in H_y or W_t compresses the slot area, but lowers the flux density in the stator core. To improve the torque performance, they need to be designed with a compromise, considering the electrical load and the saturation problem.

IV. Optimal Design

An optimization of the DFDR-PM is conducted based on a genetic algorithm (GA) and the FEM. The aim is to maximize the torque capability of the system with both the E-CVT part and the generator part considered. As the torque components due to two windings need to balance each other on the outer rotor, both of them are important and their maximum values should be similar. The fitness function is

$$F(H_{\mathrm{ri}}, H_{\mathrm{ro}}, R_s, H_y, W_t) = T_{\mathrm{ro1}} \cdot T_{\mathrm{ro2}}. \tag{13}$$

The following constraints are used for the optimization:

1) The outer geometry is fixed. The outer diameter of the stator is 216 mm and the stack length is 65 mm.

TABLE I
Specifications of the DFDR-PM

	Quantity	Value
DFDR-PM	Outer radius of stator	108.0 mm
	Inner radius of stator	74.7 mm
	Inner airgap length	1.0 mm
	Radial length of outer rotor	6.1 mm
	PM length of inner rotor	15.8 mm
	PM pole-pair number in outer rotor	28
	PM pole-pair number in inner rotor	17
	Number of stator slots	48
	Stack length	65 mm
	Stator and rotor core material	M19_24G
	Magnetic remanence	1.2 T
	Rated efficiency at synchronous speed	70%
	Power density	7.0×10^2 kW/ m^3
E-CVT part	Pole-pair number of the primarywinding	11
	Rated inner rotor torque	27 Nm
	Rated current of the primary winding	11.5 A
	Rated efficiency	76%
Generator part	Pole-pair number of secondarywinding	28
	Rated frequency	50 Hz
	Rated outer rotor torque	44.5 Nm
	Rated output phase voltage	13.5 V(rms)
	Rated output phase current	10.4 A(rms)
	Rated efficiency	86%

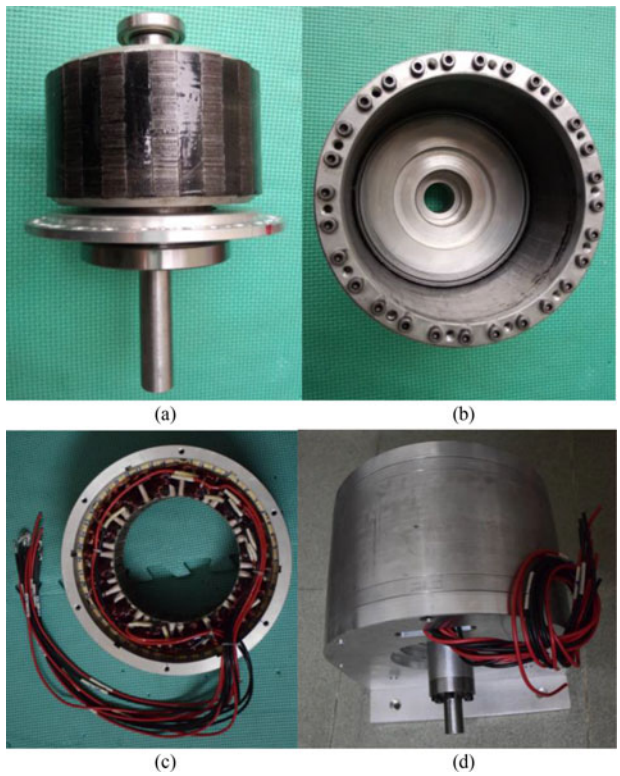

Fig. 8. (a) The inner rotor; (b) the outer rotor; (c) the stator; (d) the whole prototype of the DFDR-PM.

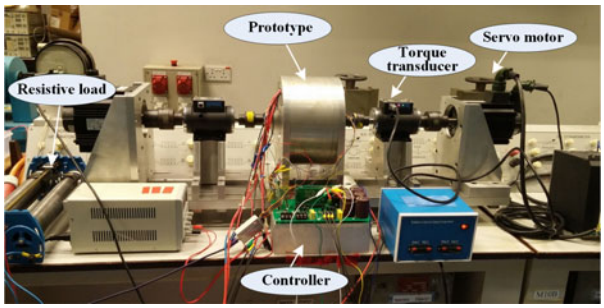

Fig. 9. Test bed.

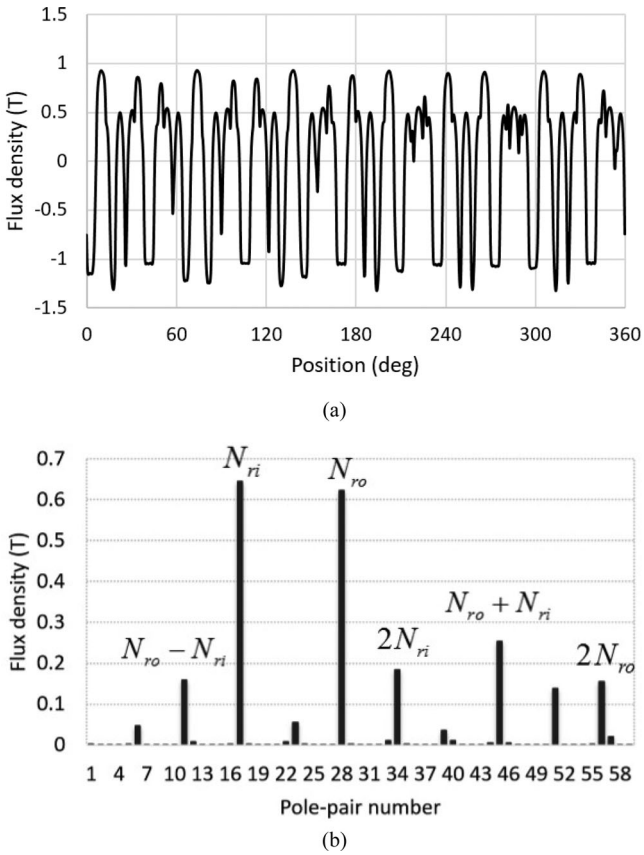

Fig. 10. (a) PM flux density in the inner airgap and (b) corresponding spectra.

2) The lengths of the outer airgap and the inner airgap are both fixed at 1 mm.
3) The current density in the conductor is limited within 5.5 A/mm^2. The slot fill factor, which is the ratio of the cross-section area of conductors to the slot area, is 55%.

For each element, T_{ro1} and T_{ro2} are computed using transient FEM analysis, respectively. Unlike the parametric analysis in which the windings are excited separately, to have the saturation issue considered, both windings are excited in the optimization. For the calculation of T_{ro1}, the locked-rotor torque angle curve is first computed with the primary winding excited with ac current and the secondary winding excited with dc current. By averaging the maximum value and the minimum value in the torque angle curve, the torque component due to the secondary winding can be removed and T_{ro1} is calculated. The torque T_{ro2} can be calculated in a similar way

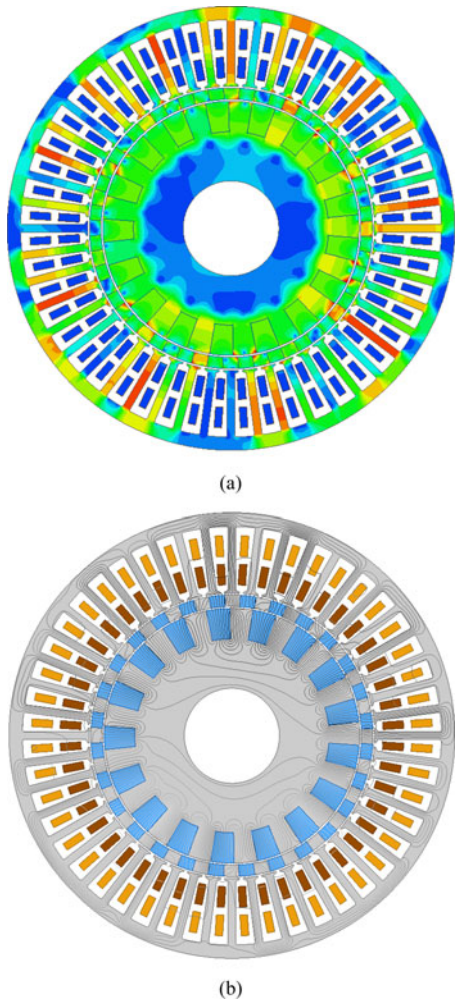

Fig. 11. (a) Flux density map and (b) flux line plot at the rated load.

by exciting the primary winding with dc current and the secondary winding with ac current. A flowchart of the optimization process is shown in Fig. 6.

The optimization is conducted with the following considerations: a population of 30 elements, the maximum generation number of 20, crossover probability of 0.8, and mutation probability of 0.1.

To improve the GA convergence performance, for each gener-ation, if the best element is worse than the best element of its pre-vious generation, its worst element will be replaced by the pre-vious best element. The fitness variation during the optimization process is shown in Fig. 7. Although the average fitness of the population goes up and down, the best fitness keeps increasing. The optimized variables are $H_{\mathrm{ri}} = 15.8$ mm, $H_{\mathrm{ro}} = 6.1$ mm, $R_{\mathrm{s}} = 73.3$ mm, $H_{\mathrm{y}} = 4.1$ mm, and $W_t = 3.9$ mm. Through the optimization, the slot area is designed to be relatively large. This is due to the arrangement of placing both windings in one stator. The other specifications of the DFDR-PM are listed in Table I.

V. Performance Validation

To validate the performance of the proposed machine, besides FEM simulation, a prototype is also made and tested as shown in Figs. 8 and 9. The inner rotor of the prototype is connected to a

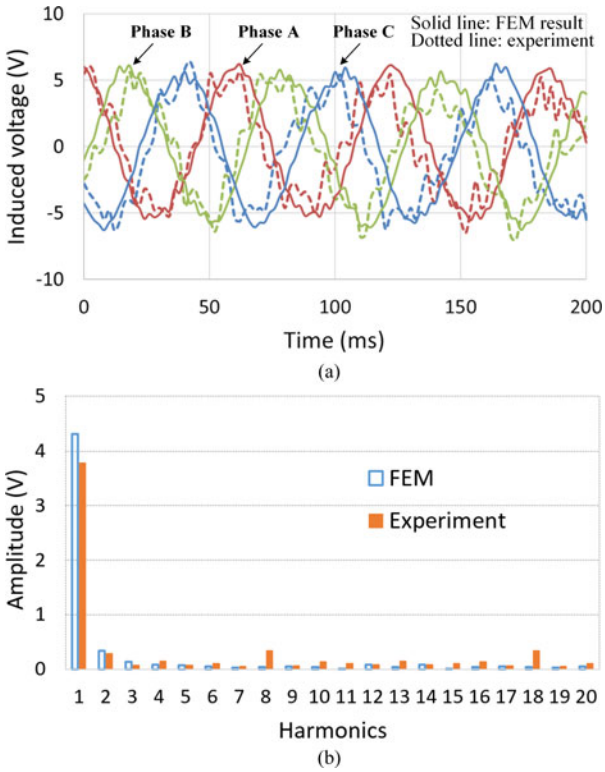

Fig. 12. (a) Back EMF during subsynchronous operation in the primary winding and (b) corresponding harmonic spectra.

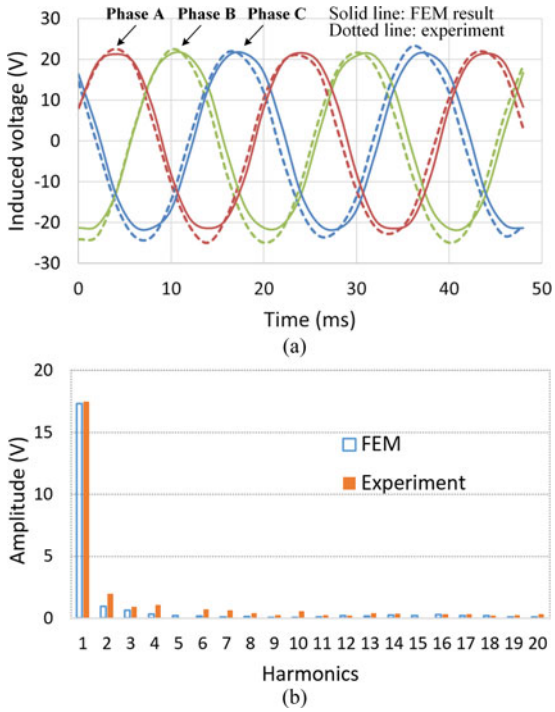

Fig. 13. (a) Back EMF during subsynchronous operation in the secondary winding and (b) corresponding harmonic spectra.

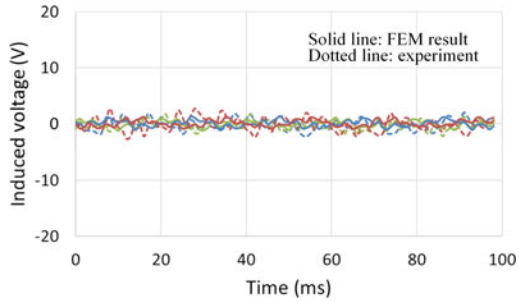

Fig. 14. Back EMF during synchronous operation in the primary winding.

servo motor through a torque transducer. The primary winding is connected to the controller and the secondary winding is connected to resistive load.

A. Field and Back EMF

Using FEM, the PM field is computed. The airgap flux density and the corresponding spectra are depicted in Fig. 10. Besides the largest fundamental components N_{ri} and N_{ro} , four harmonic components $2N_{\mathrm{ri}}$, $2N_{\mathrm{ro}}$, $N_{\mathrm{ro}} - N_{\mathrm{ri}}$, and $N_{\mathrm{ro}} + N_{\mathrm{ri}}$ are also significant. These FEM results agree well with the theoretical analysis given in Section II. Under the rated load, the magnetic flux density and the flux lines are plotted in Fig. 11. The maximum flux density is about 2 T, which is acceptable for the silicon steel used.

The back EMFs in two sets of windings during subsynchronous and synchronous operation and the corresponding harmonic spectra are shown in Figs. 12–15. For subsynchronous operation, the speed of the inner rotor is set at 120 r/min.

For subsynchronous operation, the frequency of the back EMF in the primary winding is around 16 Hz, which corresponds with the theoretical analysis (7). The ripples in the back EMF of the primary winding by FEM are mainly due to the slot effect. As the back EMF of the primary winding has a small amplitude in this analysis, its waveform is easier to be affected than that of the secondary winding.

1) The experimental and FEM results are generally in agreement, especially for the secondary winding back EMF. In Fig. 12(a), the experiment result has larger distortion than the FEM result. The possible reasons are the small ripples in the inner rotor speed during the test. Also, the back EMF of the primary winding is easier to be affected since its magnitude is small.
2) During synchronous operation, the back EMF in the primary winding is close to zero. The reason is that the speed of the effective harmonic component is zero according to (6).
3) When the speed of the inner rotor changes from subsynchronous to synchronous, the back EMF in the secondary winding is constant while the back EMF in the primary winding changes accordingly. In the WECS, when the current frequency of the primary winding is intentionally controlled to vary with the speed of the inner rotor, the outer rotor speed can be kept constant and hence the output voltage can be kept constant, which realizes the VSCF operation.

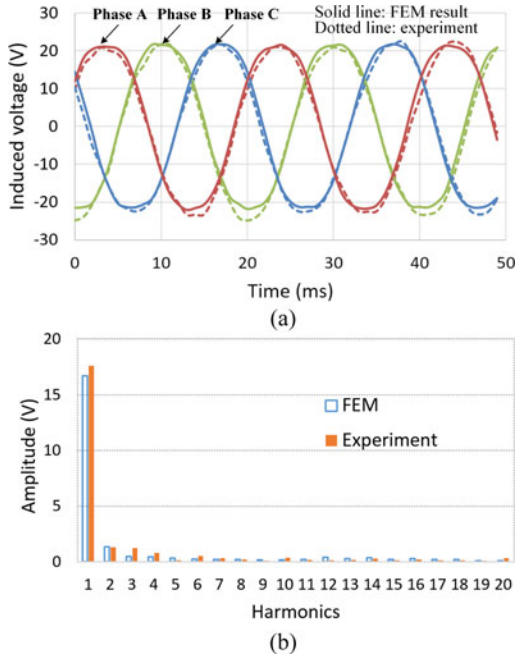

Fig. 15. (a) Back EMF during synchronous operation in the secondary winding and (b) corresponding harmonic spectra.

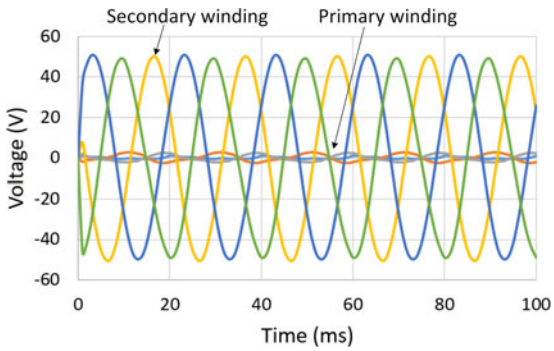

Fig. 16. Induced voltages in the primary and secondary windings when the secondary winding is excited.

When the rotors are fixed and a current of 50 Hz is applied to the secondary winding, the induced voltages in both windings are shown in Fig. 16. It can be seen that, compared with the self-inductances of the secondary winding, the mutual inductances between the primary and secondary windings are nearly negligible.

B. Operation Under Load Conditions

At first, the performances of the E-CVT part and the generator part are tested separately. For the test of the E-CVT part, the outer rotor is locked and the inner rotor is driven by the primary winding. At different inner rotor speeds and torque loads, the losses and efficiency are shown in Fig. 17. The copper loss is calculated simply by Joule's first law and it increases with the winding current. The sum of coreloss and the mechanical loss are measured by reducing the copper loss from the total loss. This part of losses increases with both the load torque and the rotor speed. For the generator part test, the outer rotor is driven by a servo motor and the secondary winding is connected to a resistive load. The losses and efficiency of the generator part are shown in Fig. 18.

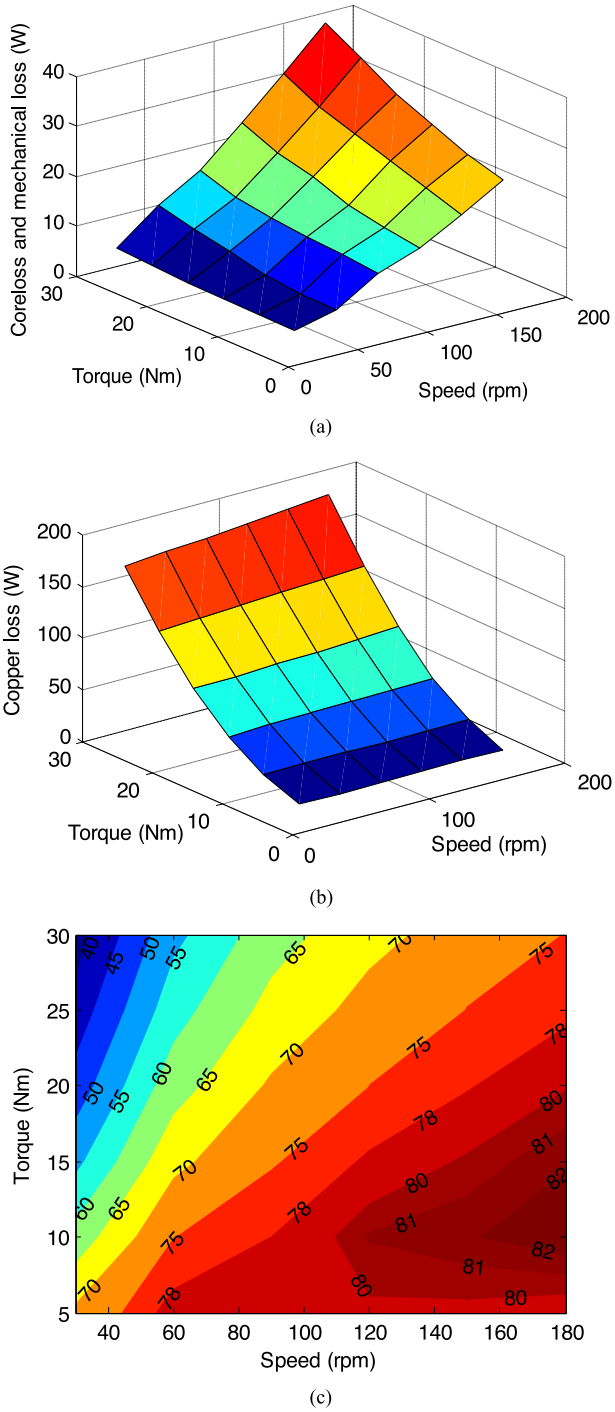

Fig. 17. (a) Coreloss and mechanical loss, (b) copper loss, and (c) efficiency of the E-CVT part at different inner rotor speeds and torque.

When both the primary winding and secondary winding are used to drive the outer rotor, the outer rotor torque with respect to different winding currents is analyzed using FEM and shown in Fig. 19. It can be seen that the outer rotor torque is decided by the currents of both the primary and the secondary windings.

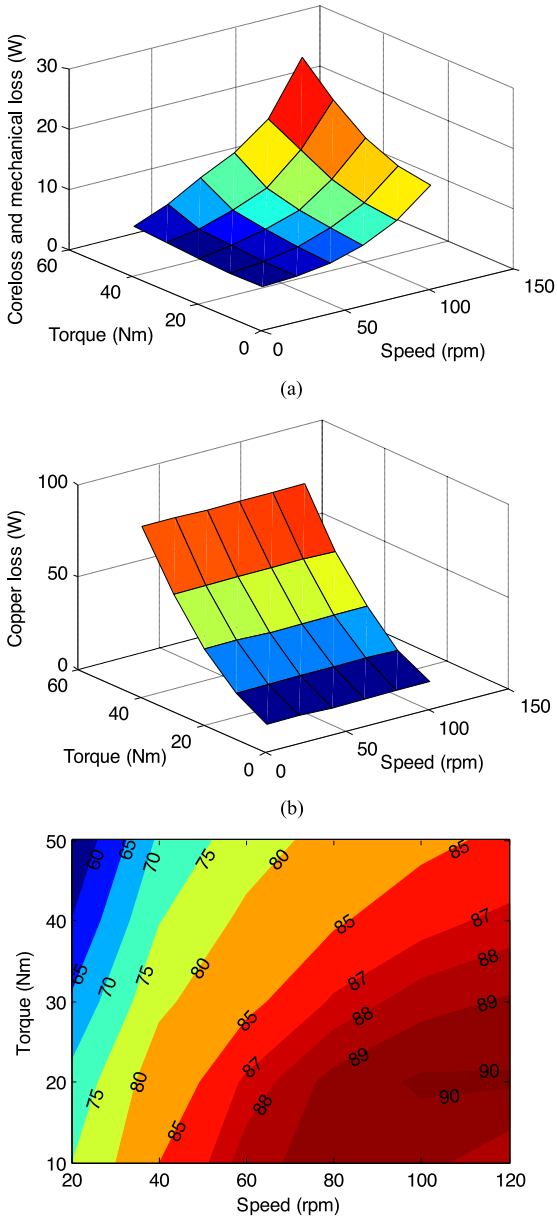

Fig. 18. (a) Coreloss and mechanical loss, (b) copper loss, and (c) efficiency of the generator part at different outer rotor speeds and torque.

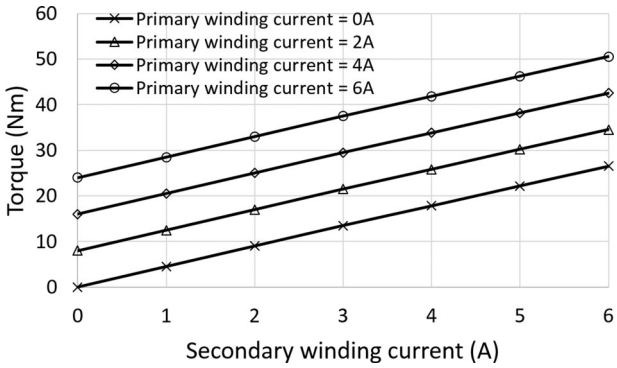

Fig. 19. Outer rotor torque at different winding currents.

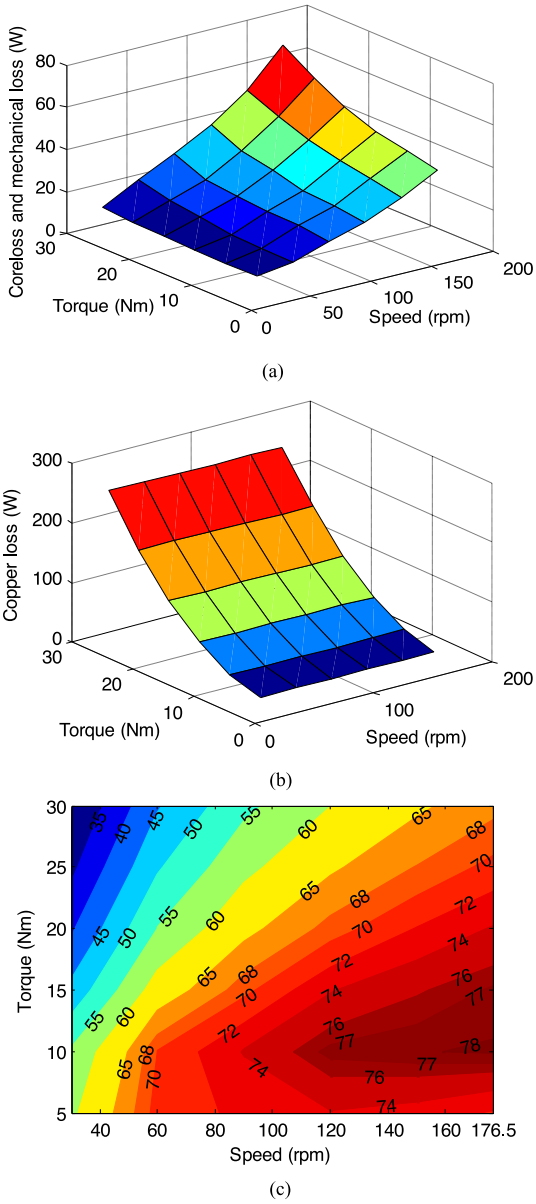

Fig. 20. (a) Coreloss and mechanical loss, (b) copper loss, and (c) efficiency of the DFDR-PM at different inner rotor speeds and torque.

For the test of the DFDR-PM, the secondary winding is connected to a resistive load. The inner rotor is driven by a servo motor at different speeds, while the outer rotor speed is kept constant, namely 107 r/min, by the primary winding. Assuming the efficiency of the converter to be 1, the losses and efficiency of the DFDR-PM under different input speeds and torques from the servo motor are shown in Fig. 20. The efficiency is calculated by

$$\eta = \frac{3UI}{T_{\mathrm{mec}}\omega_2 + 3U_{\mathrm{con}}I_{\mathrm{con}}\cos\phi} \tag{14}$$

where U and I are the output voltage and current of the secondary winding; T_{mec} is the output torque of the servo motor; U_{con}, I_{con}, and ϕ are the output voltage, current, and phase angle difference of the controller.

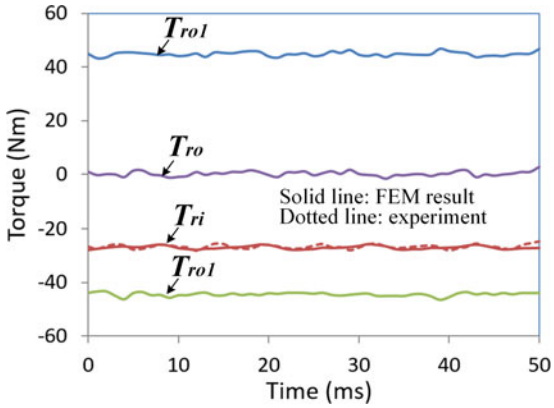

Fig. 21. Electromagnetic torque of two rotors.

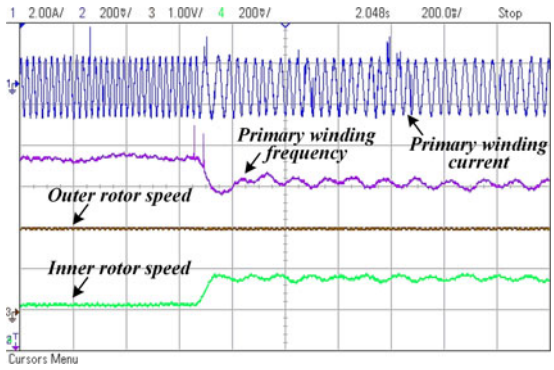

Fig. 22. System dynamics when the inner rotor speed changes.

When the inner rotor is at 120 r/min and the outer rotor is at 107 r/min stably under the rated load, the torque on the inner rotor is measured in comparison with FEM analysis results, as shown in Fig. 21.

1) As we have considered the cogging torque factor for the design of the pole number combination, the torque ripple is generally acceptable.
2) For the outer rotor, the torque due to the primary winding and the torque due to the secondary winding are canceling each other, which makes it a floating rotor.
3) The electromagnetic torque of the inner rotor is to be cancelled out by the mechanical torque from the wind blades in the WECS. In this experiment, it is balanced by the servo motor instead.

A simple test for the dynamics of the system in VSCF operation is also conducted, as shown in Fig. 22. Obviously, when the inner rotor speed increases, the frequency of the controlled current in the primary winding decreases so that the speed of the outer rotor is kept constant.

VI. Conclusion

A novel WECS concept based on E-CVT was proposed for VSCF wind power generation. The basic idea is to realize variable-speed operation by compensating the power from the wind turbine. Utilizing the flux-modulation effect among the windings and rotors, the frequency of the output voltage is decoupled from the wind turbine speed. By artfully integrating a flux-modulation machine with a conventional PM machine, this system realizes the speed matching and power generation within one single machine. Compared with previous WECS concepts, this system has the advantages of being gearless and brushless and it needs only a partial-scale converter, which means to incorporate the merits of the popular DFIG system and direct-drive PMSG system. The working principle and design of the core DFDR-PM were introduced. The performance of the DFDR-PM was validated by both FEM simulation and experimental results.

Acknowledgment

The authors would like to acknowledge and thank Dr. X. Luo for his contribution to the experimental verification.

References

[1] H. Polinder, J. A. Ferreira, B. B. Jensen, A. B. Abrahamsen, K. Atallah, and R. A. McMahon, "Trends in wind turbine generator systems," *IEEE J. Emerg. Sel. Topics Power Electron.*, vol. 1, no. 3, pp. 174–185, Sep. 2013.

[2] M. Liserre, R. Cardenas, M. Molinas, and J. Rodriguez, "Overview of multi-MW wind turbinesand wind parks," *IEEE Trans. Ind. Electron.*, vol. 58, no. 4, pp. 1081–1095, Apr. 2011.

[3] J. K. Kaldellis and D. Zafirakis, "The wind energy (r)evolution: A short review of a long history," *Renewable Energy*, vol. 36, no. 7, pp. 1887–1901, Jul. 2011.

[4] H. Gorginpour, H. Oraee, and R. A. McMahon, "Electromagnetic-thermal design optimization of the brushless doubly-fed induction generator," *IEEE Trans. Ind. Electron.*, vol. 61, no. 4, pp. 1710–1721, Apr. 2014.

[5] V. Yaramasu, B. Wu, P. C. Sen, S. Kouro, and M. Narimani, "High-power wind energy conversion systems: State-of-the-art and emerging technologies," *Proc. IEEE*, vol. 103, no. 5, pp. 740–788, May 2015.

[6] E. Camm *et al.*, "Characteristics of wind turbine generators for wind power plants," in *Proc. IEEE Power Energy Soc. Gen. Meet.*, Calgary, AB, Canada, Jul. 2009,pp. 1–5.

[7] C. Rossi, P. Corbelli, and G. Grandi, "W-CVT continuously variable transmission for wind energy conversion system," in *Proc. IEEE Conf. Power Electron. Mach. Wind Appl.*, Jun. 2009, pp. 1–10.

[8] K. Atallah, J. B. Wang, S. D. Calverley, and S. Duggan, "Design and operation of a magnetic continuously variable transmission," *IEEE Trans. Ind. Appl.*, vol. 48, no. 4, pp. 1288–1295, Jul./Aug. 2012.

[9] X. Sun, M. Cheng, Y. Zhu, and L. Xu, "Application of electrical variable transmission in wind power generation system," *IEEE Trans. Ind. Appl.*, vol. 49, no. 3, pp. 1299–1307, May/Jun. 2013.

[10] K. Atallah, S. D. Calverley, and D. Howe, "Design, analysis and realization of a high-performance magnetic gear," *Proc. Inst. Elect. Eng.—Elect. Power Appl.*, vol. 151, no. 2, pp. 135–143, Mar. 2004.

[11] Z. Q. Zhu, Z. P. Xia, L. J. Wu, and G. W. Jewell, "Influence of slot and pole number combination on radial force and vibration modes in fractional slot PM brushless machines having single and double layer windings," in *Proc. IEEE Energy Convers. Congr. Expo.*, Sep. 2009, pp. 3443–3450.

[12] B. Prieto, M. Martinez-Iturralde, L. Fontan, and I. Elosegui, "Analytical calculation of the slot leakage inductance in fractional-slot concentrated-winding machines," *IEEE Trans. Ind. Electron.*, vol. 62, no. 5, pp. 2742–2752, May 2015.

[13] S. Niu, S. L. Ho, and W. N. Fu, "Design of a novel electrical continuously variable transmission system based on harmonic spectra analysis of magnetic field," *IEEE Trans. Magn.*, vol. 49, no. 5, pp. 2161–2164, May 2013.

[14] Z. Q. Zhu and D. Howe, "Influence of design parameters on cogging torque in permanent magnet machines," *IEEE Trans. Magn.*, vol. 15, no. 5, pp. 407–412, May 2000.

[15] M. G. Say, *Performance and Design of AC Machines*, 3rd ed. London, U.K.: Pitman, 1968.

[16] B. Kim and T. A. Lipo, "Operation and design principles of a PM vernier motors," *IEEE Trans. Ind. Appl.*, vol. 50, no. 6, pp. 3656–3663, Nov./Dec. 2014.

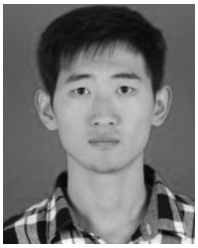

Yulong Liu received the B.Sc. degree in electrical engineering from Zhejiang University, Hangzhou, China, in 2012. He is currently working toward the Ph.D. degree in electrical engineering at The Hong Kong Polytechnic University, Kowloon, Hong Kong.

From April to August 2015, he was a Research Scholar with the Department of Neurosurgery, University of Pittsburgh, Pittsburgh, PA, USA. His research interests include electric machines, electric vehicles, renewable power generation, and applied electromagnetics.

Shuangxia Niu received the B.Sc. and M.Sc. degrees in electrical engineering from the School of Electrical Engineering and Automation, Tianjin University, Tianjin, China, in 2002 and 2005, respectively, and the Ph.D. degree in electrical engineering from the Department of Electrical and Electronic Engineering, The University of Hong Kong, Hong Kong, in 2009.

Since 2009, she has been with The Hong Kong Polytechnic University, Kowloon, Hong Kong, where she is currently an Assistant Professor in the Department of Electrical Engineering. She has authored or coauthored over 70 conference papers and more than 50 papers in leading journals. Her research interests include the design and control of novel electrical machines and drives, renewable energy conversion systems, and applied electromagnetics.

Weinong Fu received the B.Eng. degree in electrical engineering from Hefei University of Technology, Hefei, China, the M.Eng. degree in electrical engineering from Shanghai University of Technology, Shanghai, China, and the Ph.D. degree in electrical engineering from The Hong Kong Polytechnic University, Kowloon, Hong Kong, in 1982, 1989, and 1999, respectively.

He is currently a Professor with The Hong Kong Polytechnic University. Before joining the university in October 2007, he was one of the key developers at Ansoft Corporation, Pittsburgh, PA, USA. He has about seven years of working experience at Ansoft, focusing on the development of the commercial software Maxwell. He has published 184 papers in refereed journals. His current research interests include numerical methods of electromagnetic field computation, optimal design of electric devices based on numerical models, applied electromagnetics, and novel electric machines.